PAPER • **OPEN ACCESS**

The impact of neon seeding on pedestal performance and stability of JET-ILW deuterium H-mode discharges

Plasma Physics and Controlled Fusion

OPEN ACCESS

RECEIVED
24 September 2025

REVISED
24 November 2025

ACCEPTED FOR PUBLICATION
16 December 2025

PUBLISHED
14 January 2026

PAPER

The impact of neon seeding on pedestal performance and stability of JET-ILW deuterium H-mode discharges

M Šos[1,2,*], C Giroud[3], L Frassinetti[4], B Chapman-Oplopoiou[3], S Saarelma[3], D B King[3], S Wiesen[5], B Labit[6], A Kappatou[7], D Keeling[3], N Vianello[8], M Wischmeier[7], A Boboc[3], J M Fontdecaba Climent[9], Z Huang[3], D Kos[3], E Litherland-Smith[3], J Macdonald[3], S Menmuir[3], G Szepesi[3], ITER-baseline team[10], JET Contributors[11] and the EUROfusion Tokamak Exploitation Team[12]

[1] Institute of Plasma Physics of the Czech Academy of Sciences, U Slovanky 2525/1a, 182 00 Praha 8, Czech Republic
[2] Faculty of Nuclear Sciences and Physical Engineering, Czech Technical University in Prague, Brehova 7, Praha 1, Czech Republic
[3] UKAEA, United Kingdom Atomic Energy Authority, Culham Campus, Abingdon OX14 3DB, United Kingdom
[4] Division of Electromagnetic Engineering and Fusion Science, KTH Royal Institute of Technology, Stockholm SE-11428, Sweden
[5] Forschungszentrum Jülich GmbH, Institut für Energie- und Klimaforschung, Plasmaphysik, 52425 Jülich, Germany
[6] Ecole Polytechnique Fédérale de Lausanne, Swiss Plasma Center, CH-1015 Lausanne, Switzerland
[7] Max Planck Institute for Plasma Physics, Boltzmannstrasse 2, 85748 Garching bei München, Germany
[8] Consorzio RFX, Corso Stati Uniti 4, 35127 Padova, Italy
[9] Laboratorio Nacional Fusión, CIEMAT, Av Complutense 40, 28040 Madrid, Spain
[10] See Giroud C *et al* 2025 30th IAEA Fusion Energy Conference for the JET-ITER baseline team.
[11] See Maggi *et al* 2024 (https://doi.org/10.1088/1741-4326/ad3e16) for the JET Contributors.
[12] See Joffrin *et al* 2024 (https://doi.org/10.1088/1741-4326/ad2be4) for the EUROfusion Tokamak Exploitation Team.
[*] Author to whom any correspondence should be addressed.

E-mail: sos@ipp.cas.cz

Keywords: tokamak, JET, neon seeding, pedestal, ideal MHD

Abstract

This work presents a systematic study of the impact of neon seeding on pedestal performance and stability in JET-ITER baseline scenario discharges in deuterium at high input power, extending previous JET impurity seeding experiments. A neon-seeding scan of the JET-ITER baseline at $I_p = 2.5$ MA, $B_T = 2.7$ T, $q_{95} = 3.2$ with high triangularity is studied with a neon pedestal concentration up to 1.7% at the pedestal top. As is typical in these discharges, the global confinement is increased approaching unity and the β_N parameter reaches up to 2.3 with the increased radiation fraction. A detailed pedestal profile analysis showed that neon seeding reduces the pedestal density while substantially increasing both the electron and ion pedestal temperatures, resulting in an overall ∼50% increase in pedestal pressure compared to unseeded plasmas. Simultaneously, the total pressure pedestal width broadens, mostly due to the increased T_e width (n_e broadening has a negligible impact on the total pressure width). The total pressure gradient develops in a way that stabilizes the pedestal against ideal peeling–ballooning (PB) modes. Ideal magnetohydrodynamics (MHD) stability calculations confirm that unseeded pedestals lie close to the PB boundary, while neon-seeded cases move deep into the PB stable domain, consistent with the observed transition to small or no edge-localized mode (ELM) operation. Comparison with the Europed predictions exhibits good qualitative agreement in pedestal height trends, though systematic offsets and the underestimation of pedestal widths highlight the limitations of the current model.

1. Introduction

Impurity seeding is a powerful tool that may help to protect the plasma-facing components of a tokamak-like device by reducing the heat flux via enhanced radiation in the divertor region [1, 2]. At the same time, degradation of plasma energy confinement must be avoided, which highlights the importance of studying the impact of increasing impurity levels on the pedestal pressure and its stability [3]. Multiple studies on JET [1], ASDEX Upgrade [2], Alcator C-Mod [4], and DIII-D [5, 6] tokamaks have demonstrated that low-Z impurity seeding can strongly modify the pedestal structure.

Over the past few years, JET has addressed this issue for the baseline ITER scenario, the so-called JET-ITER baseline scenario, in order to demonstrate an integrated baseline scenario in the high-performance regime with high confinement quality ($H_{98} \sim 1$) using a neon-seeded radiative divertor [1, 7–10]. Contrary to previous expectations, in some cases the presence of impurities leads to an actual improvement in pedestal pressure and energy confinement. Moreover, the results suggest comparable improvements in the global performance of neon seeding compared with nitrogen seeding, which is not considered for ITER due to the potential risk of tritiated ammonia formation [7, 11].

Extensive studies have shown that high confinement quality ($H_{98} \sim 1$) and partially detached divertor conditions are only possible for highly fueled plasmas, achieved by improving the pedestal pressure and temperature with impurity seeding, particularly in the case of neon [7].

The goal of this contribution is to assess the performance of the JET-ITER baseline scenario from the latest high-power, high-performance experimental campaign with neon seeding in deuterium. This study provides a comprehensive analysis of how neon seeding affects the pedestal structure and stability, offering insights into the interplay between pedestal current, stability limits, and ELM behavior. The paper begins by describing the dataset of discharges examined (section 2), followed by detailed profile analyses to characterize changes in the pedestal height, width, and gradient with neon seeding (section 3). In section 4, the impact on pedestal stability is evaluated using ideal MHD calculations. Section 5 compares the experimental observations with predictive results from the Europed code, providing insight into the applicability of these results for core–edge integrated modeling. Finally, the findings are summarized and discussed in section 6 in the broader context of impurity seeding.

2. Dataset description

Our dataset comprises deuterium-fueled JET-ITER baseline scenario discharges with the ITER-like wall at $q_{95} \approx 3.2$, high triangularity ($\delta \sim 0.36$[13]), and input power P_{in} in the high-power range typical of recent JET Ne-seeding campaigns. As summarized in table 1, the dataset is characterized by a relatively high plasma current of $I_p \approx 2.5$ MA and toroidal magnetic field $B_T \approx 2.7$ T. The external heating power is varied due to the availability of given power sources, $P_{abs} \approx 30$–34 MW. Deuterium fuel gas puffing is kept constant during the scan, at $\Gamma_D \approx 3.7{\cdot}10^{22}$ e s^{-1}. The strike points are located on vertical tiles. Discharges #103398 and #105625 serve as unseeded reference cases for the rest of the scan, and are designed to see the impact of the gradual increase in the neon gas inflow Γ_{Ne} towards detachment. The average neon concentration $< C_{Ne} >$ thus increases gradually going from the unseeded cases to the most seeded discharge #103185, reaching 1.66% of neon concentration at the radial location close to the pedestal top. The neon concentration was estimated by means of the charge exchange radiation spectroscopy (CXRS) diagnostic observing the neon impurity [12, 13].

As the neon concentration increases, the global performance of the seeded discharges improves, as shown also in [1, 7]. Significant improvement in the confinement quality is observed, with β_N rising from 1.17 to 2.25 due to the increasing total plasma pressure as the magnetic field and plasma current remain constant, as shown in figure 1 (left). Moreover, a steady increase in the H_{98} factor from 0.65 up to 0.92 is observed; see figure 1 (right). Correction to the fast particle contribution was included during the calculation of H_{98}. The radiated energy fraction (f_{rad}) increases gradually with the neon concentration transferring from the attached plasma to an early detachment phase. The assessment of the detachment quality and its impact on the pedestal structure and stability is outside the scope of this contribution. It is noteworthy that while higher neon radiation might be expected to reduce the power crossing the separatrix, P_{sep}[14], and thus the confinement quality, the seeded discharges instead reach stronger pedestals and higher stored energy, resulting in improved confinement quality at elevated P_{sep}. Here, P_{sep} is evaluated in the pre-ELM phase. Firstly, the input power P_{in} was increased at higher levels of neon seeding, which was proven necessary to avoid degradation of the discharge performance in a previous study [1]. Additionally, in the unseeded cases, dW/dt remains significant because the stored energy W continues to evolve until the ELMs occur, while in the mitigated or ELM-free seeded plasmas the effective dW/dt is reduced. The radiated power from the core plasma, P_{rad}, also increases with the increasing neon concentration, but less strongly than the combined effect of $P_{in} - dW/dt$. As a result, the net P_{sep} increases overall. Earlier studies [9, 14] indicate that the primary driver of the observed increase of P_{sep} and improvement of confinement quality is the development of higher pedestal temperature, and

[13] Calculated as an average of upper and lower triangularity: $\delta_{upper} \approx 0.34 - 0.37$, $\delta_{lower} \approx 0.34 - 0.35$.

[14] P_{sep} was calculated as $P_{in} - dW/dt - P_{rad}$, where P_{in} is the input power, dW/dt refers to the change in stored plasma energy and P_{rad} is the radiated power from the confined plasma region ($\psi_N < 1.0$).

Table 1. Relevant plasma parameters of presented JET-ILW dataset, namely discharge number, time window for profile selection, plasma current I_p, toroidal magnetic field strength B_T, total external heating power P_{abs}, heat flux crossing the separatrix P_{sep}, rate of deuterium gas injection Γ_D, confinement parameter β_N, rate of injected neon gas Γ_{Ne}, resulting neon concentration $< C_{Ne} >$ averaged along the view chord at radial position 3.6 m, effective charge Z_{eff}, upper and lower triangularity δ_{upper} and δ_{lower}, respectively, confinement quality factor H_{98}, and radiated energy fraction f_{rad}.

Number	Time window	I_p (MA)	B_T (T)	P_{abs} (MW)	P_{sep} (MW)	Γ_D (10^{22} e s^{-1})	β_N
103 398	[52.4622, 54.5613]	2.47	2.74	28.67	14.50	3.81	1.17
105 625	[52.3085, 53.9758]	2.47	2.74	30.49	15.05	3.61	1.24
103 179	[52.3338, 54.3570]	2.47	2.74	32.55	16.42	3.73	1.49
103 176	[51.5377, 52.9054]	2.48	2.73	31.23	17.96	3.78	1.74
103 176*	[52.9325, 54.4063]	2.47	2.74	31.99	18.71	3.75	1.82
103 184	[52.6407, 53.7334]	2.48	2.74	34.16	20.80	3.72	2.07
103 185	[51.4996, 53.5518]	2.48	2.74	34.39	21.41	3.71	2.25

#	Γ_{Ne} (10^{22} e s^{-1})	$< C_{Ne} >$ (%)	Z_{eff}	δ_{upper}	δ_{lower}	H_{98}	f_{rad}
103 398	0.00	0.13	1.42	0.339	0.352	0.56	0.35
105 625	0.00	0.05	1.46	0.339	0.344	0.57	0.39
103 179	0.62	0.94	1.90	0.345	0.341	0.62	0.59
103 176	0.99	1.32	2.19	0.356	0.351	0.75	0.65
103 176*	0.55	1.28	2.15	0.363	0.340	0.76	0.63
103 184	1.45	1.54	2.30	0.360	0.351	0.85	0.67
103 185	1.65	1.66	2.50	0.373	0.353	0.92	0.68

Two different time windows of discharge #103 176 are distinguished by * symbol.

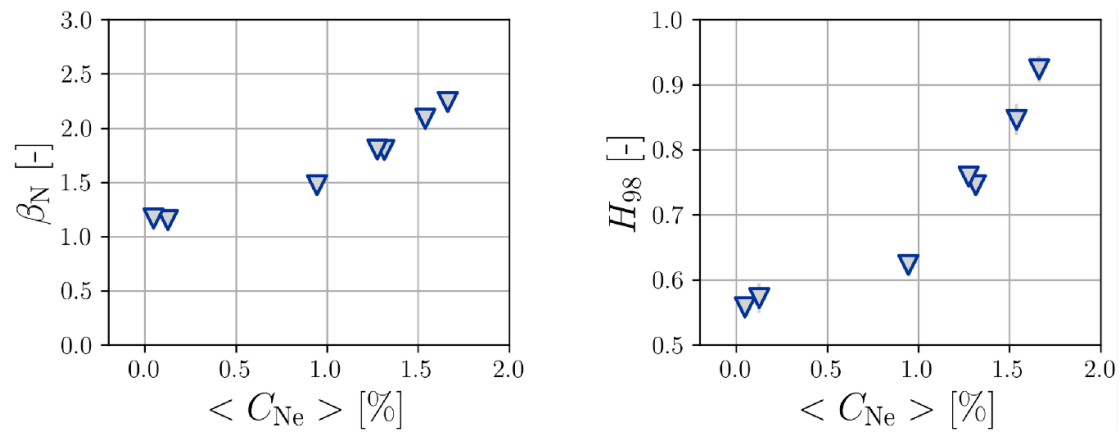

Figure 1. Correlation of parameters β_N (left) and H_{98} (right) with averaged neon concentration at the top of the pedestal $< C_{Ne} >$ for presented JET-ILW dataset.

consequently higher total pressure. Overall, the presented neon-seeded discharges demonstrate a clear enhancement of global performance with the increasing neon concentration.

Considering the ELM activity throughout the dataset, a clear transition between different ELM regimes is observed when neon seeding is applied, as shown in figure 2. Observations of the Be^{II} line radiation and divertor temperature by infrared (IR) camera suggest a decrease in both the ELM size and frequency with the increasing neon concentration, as already observed in previous JET-ILW Ne seeding research [1, 7]. In addition, the divertor temperature measured by the IR camera is lower in the neon-seeded discharges compared to the unseeded case due to the increasing f_{rad}. The presented neon-seeded JET-ITER baseline scenario does not lead to impurity accumulation with no-ELM conditions, as shown in [7, 15]. This is demonstrated in figure 3, showing the time traces of neon concentration at the top of the pedestal and deeper in the plasma center for the highly seeded discharge #103185 together with the neon gas injection rate Γ_{Ne} and line-averaged effective charge Z_{eff}, measured by means of a spectroscopic system from the background bremsstrahlung radiation. From the constant neon concentration and Z_{eff} evolution, it is clear that there is no impurity accumulation. The time window for the pre-ELM profile selection is highlighted by the gray rectangle. The energy confinement time was estimated to be $\tau_E \approx 0.2$ s within this time window; therefore, in this discharge the optimal neon concentration can be

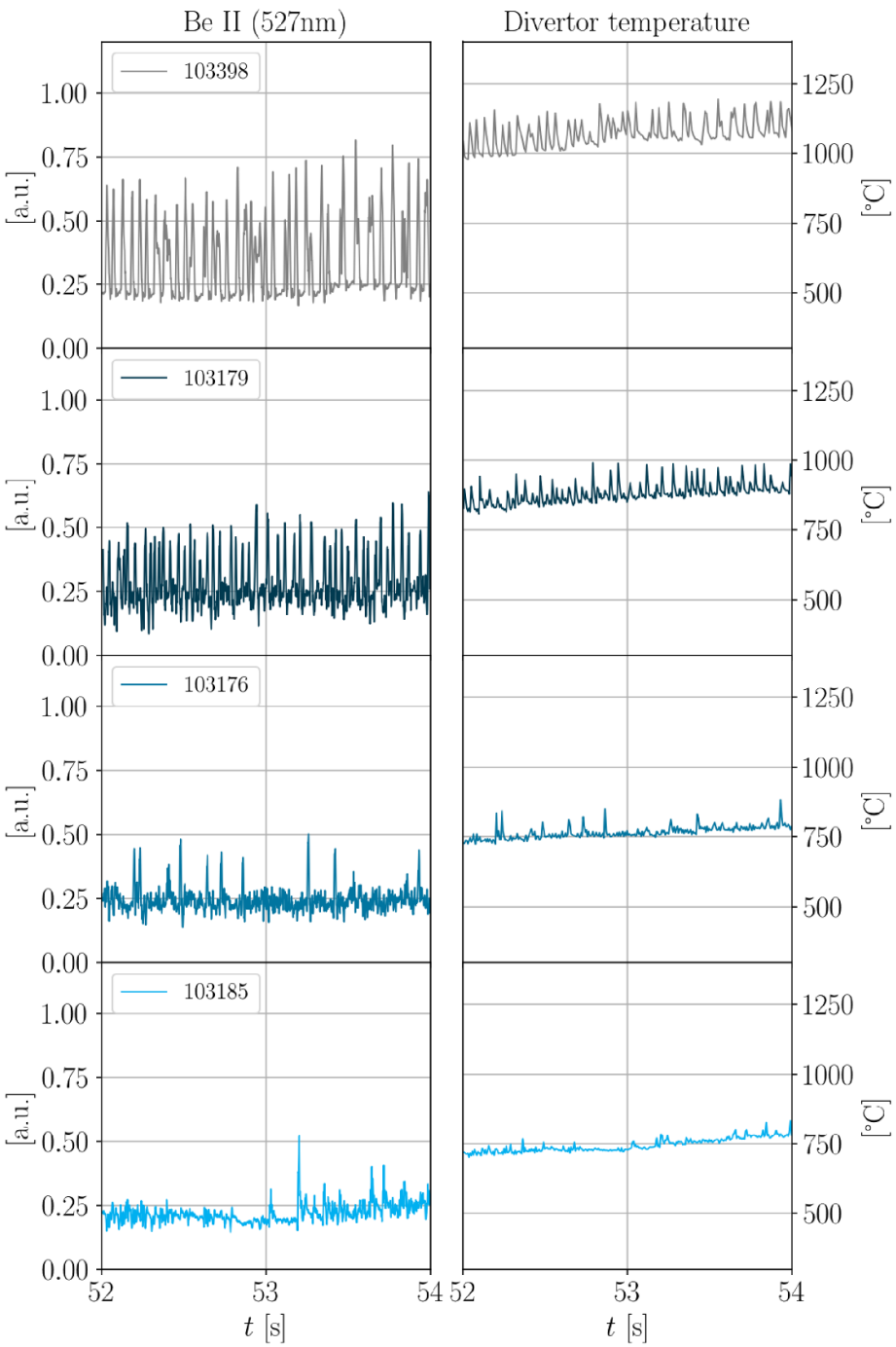

Figure 2. ELM activity characterization of multiple discharges from the presented JET-ILW dataset. (Left column) Observed signal of Be^{II} line radiation from the confined plasma region during an H-mode flat-top phase on JET tokamak discharge. Temporal averaging was applied to reduce the noise to increase the clarity of the figure. (Right column) Divertor plasma-facing component temperature measured by IR camera. Both figures show decreasing ELM activity with increasing neon seeding.

kept constant under high-performance conditions for at least five times the energy confinement time period.

This experimental and modeling study is the continuation of previously performed JET-ITER baseline scenario experiments [1] operated under a similar plasma configuration, plasma current, and magnetic field, and using a similar total injected deuterium gas rate. Despite minor differences in plasma operation (i.e. deuterium gas puffing purely from the divertor, larger gap between the plasma and the first wall in the outer region), the principal characteristics of the pedestal—namely, increasing $T_{e,i}$, decreasing n_e, and widening of the pedestals, especially the electron temperature, as discussed below—remain consistent, indicating that this represents a robust operational scenario, despite the three-year interval between the experiments.

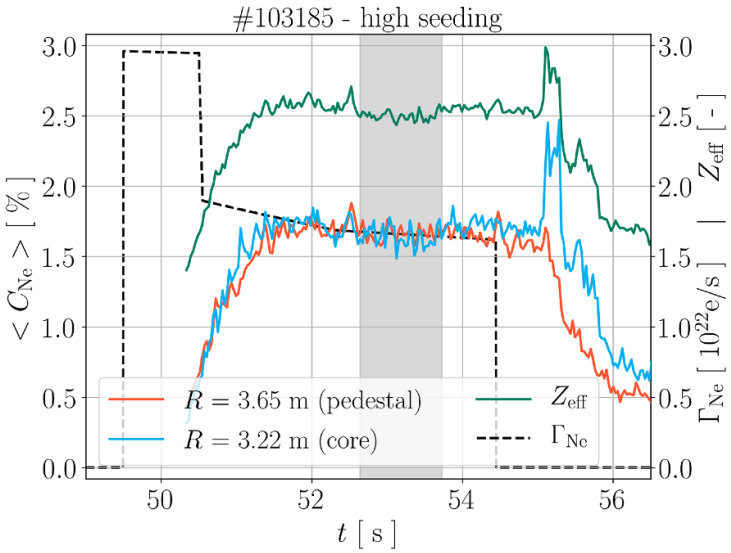

Figure 3. Time traces of the neon concentration in the plasma core (at major radius $R = 3.22$ m) and at the top of the pedestal ($R = 3.65$ m) are shown for highly seeded JET discharge #103185 together with line-integrated effective charge Z_{eff} in green and neon gas puff Γ_{Ne} in black color. Time window for the pre-ELM profile selection is highlighted by gray rectangle.

3. Pedestal structure

Characterization of the pedestal structure is necessary to understand the impact of impurity seeding on the edge plasma conditions and the mechanisms that govern pedestal behavior. In the following section, the procedure for handling kinetic profiles, i.e. profile selection and fitting, is presented. This is followed by a detailed comparison of representative experimental profiles and a description of the resulting pedestal structure.

3.1. Pedestal fitting

Measurements of the kinetic plasma profiles are provided by a set of diagnostic systems. For the purposes of this contribution, the electron density n_e and electron temperature T_e profile reconstructions were delivered by means of Thomson scattering diagnostics [16]. Ion temperature measurements were provided by CXRS diagnostics [17, 18]. Other plasma parameters were obtained using a standard set of diagnostic apparatus.

The Thomson scattering diagnostic system is able to provide instantaneous inference of radially distributed electron density and electron temperature with given spatial resolution along the laser beam path crossing the plasma cross-section. The experimental profiles were studied using the approach described in [19] and are briefly summarized here. For each discharge, a steady-state interval is selected, during which the main plasma parameters exhibit minimal variation and the ELM activity remains stable. Kinetic profiles obtained in the 70%–99% range of the ELM cycle were selected to create an aggregate profile constructed by overlaying the chosen profiles over each other using the corresponding equilibrium reconstruction to account for the proper plasma shape. The profiles are then fitted by the commonly used modified hyperbolic tangent function (1) in the pedestal region [20]. The formula for the fitting function for the electron density profile is presented below:

$$f_{n_e}(\psi) = \frac{1}{2}(n_e^{ped} - n_e^{SOL})\left(\frac{(1 + n_e^{slope}\ z)\ e^z - e^{-z})}{e^z + e^{-z}} + 1\right) + n_e^{SOL}, \quad z = \frac{n_e^{pos} - \psi}{2\ \Delta n_e}. \tag{1}$$

The pedestal parameters of a given kinetic plasma profile, such as n_e, T_e, p_{tot}, and T_i, are then extracted directly from the parameters of the fitting function shown in table 2.

A similar function is also used for fitting the total pressure p_{tot}, ion temperature T_i, and electron temperature T_e profiles, with the assumption that $T_e^{SOL} = 0$ eV. Once the profiles are properly fitted by the combined pedestal and core function, they can be compared directly to assess their characteristics. The profiles have normalized poloidal flux ψ_N as the radial coordinate, and $T_e^{sep} = 100$ eV was assumed. It was shown in several previous works [21, 22] that a variation of 20% of the value set as the separatrix temperature does not significantly affect the pedestal stability result. As discussed later, the pedestal width varies quite significantly in the presented scan, which makes using the traditional quantity for the

Table 2. Description of parameters of pedestal fitting function (1) used during the pedestal quantification process.

Parameter	Description
n_{ped}	Value at pedestal top
$n_{\mathrm{e}}^{\mathrm{SOL}}$	Value going to scrape-off layer (SOL)
$n_{\mathrm{e}}^{\mathrm{slope}}$	Value of pedestal slope going to the core
$n_{\mathrm{e}}^{\mathrm{pos}}$	Position of pedestal
Δn_{e}	Width of pedestal

pedestal height (n_{ped} parameter of the fit) as the pedestal value not adequate. It was therefore decided to use the value of the pre-ELM profile fit at the radial position of $\psi_{\mathrm{N}} = 0.85$. This representation, referred to as the *pedestal height*, is used throughout the rest of the contribution. The parameter Δn_{e}, representing the pedestal width, is used when comparing between discharges. This approach is sometimes referred to as the *full pedestal width,* and is used throughout the rest of the contribution. It should be stressed here that part of the pedestal width defined this way may be located outside the separatrix.

3.2. Pedestal structure

The impact of neon seeding on the pedestal structure can be qualitatively assessed from the direct comparison of the kinetic profiles presented in figure 4 for discharges #103398 and #103185 from the dataset. The first one, shown in black color, is the unseeded reference, while in the latter the highest level of neon seeding was applied ($\Gamma_{\mathrm{Ne}} = 1.65\ 10^{22}\,\mathrm{e\,s^{-1}}$). The electron density n_{e}, electron temperature T_{e}, total pressure p_{tot}, and ion temperature T_{i} profiles are compared in figure 4. The calculated gradients of the first three quantities are also subjected to comparison. The profile of the total plasma pressure is calculated according to

$$p_{\mathrm{tot}} = k_{\mathrm{B}}\left(n_{\mathrm{e}}T_{\mathrm{e}} + n_{\mathrm{i}}T_{\mathrm{i}}\right) \tag{2}$$

where the ion density n_{i} has been calculated as

$$n_{\mathrm{i}} = \frac{Z_{\mathrm{imp}} + 1 - Z_{\mathrm{eff}}}{Z_{\mathrm{imp}}} n_{\mathrm{e}}, \tag{3}$$

to consider the dilution effect due to the neon seeding. This was calculated using the effective charge of plasma Z_{eff} and the charge of the main impurity Z_{imp}. For the unseeded cases, the value of $Z_{\mathrm{imp}} = 2$ is used, assuming beryllium to be the main impurity. For the rest of the neon-seeded scan $Z_{\mathrm{imp}} = 10$ is assumed. It is clear from equation (2) that the electron pressure contribution is independent of the effective charge Z_{eff}, whereas the ion pressure term decreases linearly with the increasing Z_{eff}. A higher effective charge implies a larger fraction of high-Z impurity ions, leading to a reduction in the total number of ions per electron and thus a smaller ion pressure contribution. Since the ion pressure contribution scales inversely with Z_{imp}, the sensitivity of p_{tot} to variations in Z_{eff} is stronger in the unseeded ($Z_{\mathrm{imp}} = 2$) cases. In contrast, for the seeded ($Z_{\mathrm{imp}} = 10$) cases, the reduction of n_{i} with the increasing Z_{eff} is weaker. Experimentally, the observed increase of Z_{eff} implies that enhanced seeding systematically reduces the ion pressure contribution and hence lowers the total pressure. The magnitude of this reduction depends both on the impurity charge state Z_{imp} and the ion temperature T_{i}, with the strongest effect occurring when $T_{\mathrm{i}} \gg T_{\mathrm{e}}$.

Significant differences can be observed between the profiles of the two discharges, as shown in figure 4. The electron density pedestal height decreases by almost a factor of 2 while the electron temperature increases by a comparable factor. The ion temperature is increased even further in the neon-seeded case. The overall impact on the total pressure is crucial as this is an essential indicator of elevated plasma performance and confinement quality. From the increased total pressure at comparable power crossing the separatrix P_{sep}, we can assume that introducing a substantial amount of neon seeding still improves the pedestal performance, thus improving the confinement quality.

Investigating the profile parameters in detail provides a quantitative evaluation of the neon seeding impact on the pedestal structure. The findings are presented in figures 5–9, showing the dependency of the values of pedestal height, pedestal width, maximum pedestal gradients, and their positions on the average neon concentration at the top of the pedestal, respectively. Here we remind that, as defined earlier, the pedestal height is defined as the value of the pre-ELM fits at the position $\psi_{\mathrm{N}} = 0.85$. As mentioned already when figure 4 was discussed, both the electron and ion temperature pedestal heights increase significantly with the neon concentration. The electron temperature pedestal height reaches

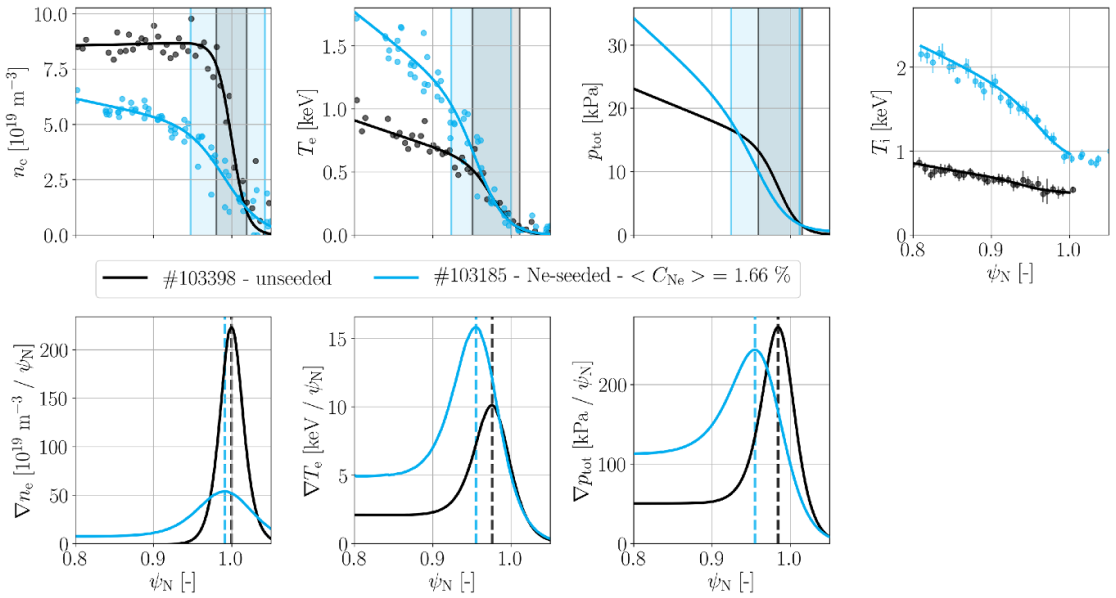

Figure 4. Kinetic plasma profiles of two selected discharges, #103398 (unseeded) and #103185 (Ne-seeded). On the top row left to right, the electron temperature T_e, electron density n_e, total plasma pressure p_{tot}, and ion temperature T_i are presented. The bottom row shows the gradient of the corresponding quantity from the first row. Instead of the gradient of ion temperature, the profile of the normalized pressure gradient is plotted. The widths of T_e, n_e, and p_{tot} are highlighted by a color span. The position of the maximum of the given profile gradient is emphasized by the vertical dashed line. Binned averaging was applied for T_i data points.

1.5 keV, which is almost twofold the unseeded case, while the ion temperatures are even higher, reaching up to 2 keV, as shown in figure 5. The electron density pedestal height decreases gradually from $\sim 9{\cdot}10^{19}\,\mathrm{m}^{-3}$ down to $\sim 6{\cdot}10^{19}\,\mathrm{m}^{-3}$ with the increasing neon concentration for average neon concentrations above 1.5%. The decrease in n_e is compensated by a significant increase in T_e, so that the overall total pressure p_{tot} increases steadily with the neon concentration by almost 50% of the unseeded reference, thus improving the confinement quality. The electron and ion pressure, p_e and p_i, respectively, highlighted in the bottom right subplot of figure 5, seem to be comparably contributing to p_{tot} for the seeded part of the presented dataset with the assumption of approximating the Z_{imp} value by the main impurity species neglecting the actual impurity mix. A significantly higher increase in T_i compared to the increase in T_e is compensated by the dilution of ion density caused by changing the Z_{imp} value from 2 to 10 and by increasing Z_{eff} with the neon seeding level (see equation (3)), reducing the overall ion pressure contribution. This experimental observation directly illustrates the analysis of equation (2) presented above.

The position of the maximum of the n_e gradient of the unseeded discharge #103398 is located very close to the separatrix, as can be observed in figure 4, and remains rather constant during the neon seeding scan as demonstrated in figure 6. However, the position of the maximum T_e gradient is further away from the separatrix for the unseeded case, creating a non-zero relative shift, which is defined as the difference between the positions of the n_e and T_e pedestals, n_e^{pos}–T_e^{pos}. With the neon concentration, T_e^{pos} is shifted inward, while the density pedestal position remains constant considering the uncertainty. The separatrix temperature is fixed to 100 eV while both the pedestal width and height are increasing. This causes a shift of the T_e pedestal top inward, and thus also its position. The position of the pedestal of p_{tot} is shifted inward, following a similar trend as observed for T_e, since the position of the density pedestal remains fairly constant. Consequently, the relative shift becomes larger with the neon concentration as well. A clear correlation between the relative shift and the ideal MHD pedestal stability results was observed for an extensive database of JET-ILW discharges [22]. Further discussions on this topic are provided in section 4.

The widths of the n_e, T_e, and p_{tot} pedestals, presented in figure 7, exhibit a consistent increase with the neon concentration, making the pedestals wider. Values are taken directly from the fitting procedure as the fitting parameter, for instance Δn_e for the electron density, to follow the systematic approach of previous research [1]. The width of the T_e pedestal increases by approximately 50% when the neon is introduced at $< C_{Ne} > \approx 1.0\%$, and then remains fairly constant, even when more neon is injected to reach 1.66% at the pedestal top. The density width Δn_e exhibits qualitatively similar behavior to ΔT_e; however, it seems to be subjected to a larger scatter throughout the seeding scan.

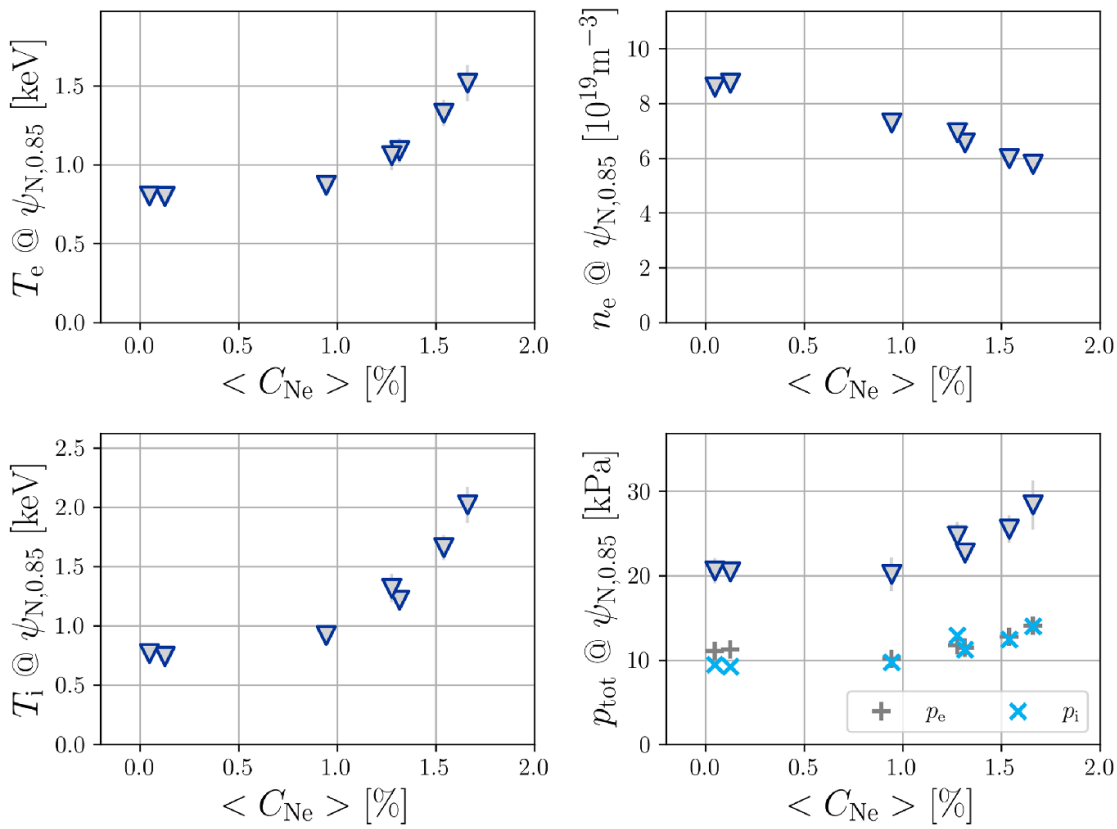

Figure 5. The correlation of pedestal height of kinetic profiles and estimated neon concentration for presented dataset. Values of electron temperature T_e, electron density n_e, ion temperature T_i, and total plasma pressure p_{tot} are presented in individual subplots. Electron p_e and ion p_i pressure contributions are highlighted.

The width of the total pressure pedestal is also estimated from the fitting of the resulting p_{tot} profile, and shows a consistent increase with the neon concentration as a result of widening both the density and temperature pedestals, as seen in figure 7. However, when we consider the inward shift of the electron temperature pedestal and the constant position of the density pedestal, it is clear that the major impact on the pedestal total pressure widening is caused by the widening of the T_e pedestal. The widening of the density width plays a negligible role because the density position is near or outside the separatrix, where the pressure gradient is already very low. The study presented here was performed by fixing the separatrix electron temperature at $T_{e,sep} = 100$ eV following the approach in most JET pedestal studies [22]. Implementing the method of calculating $T_{e,sep}$ for each particular case employing the technique based on the scrape-off layer power balance [23] to improve the consistency is outside the scope of this contribution.

Correlation of the pressure width Δp_{tot} with $\beta_{p,ped}$ does not follow the standard scaling $\Delta p_{tot} = c_{\Delta p_{tot}} \beta_{p,ped}^{1/2}$ with the coefficient equal to 0.076 [24], where $\beta_{p,ped}$ is the poloidal β at the pedestal top (here we use p_{tot} at the position $\psi_N = 0.85$). Here we remind that β_N, and consequently also $\beta_{p,ped}$, is increasing with the neon concentration in the presented scan, as shown in figure 1 (left). It is clear that no single value of the coefficient is able to properly capture the widening of the neon-seeded pedestals if the unseeded cases are included in the scaling, as presented in figure 8. The value of coefficient $c_{\Delta p_{tot}} = 0.130$ shows better agreement with the estimated pressure pedestal widths of the neon-seeded part. The coefficient values between 0.076 and 0.094 fit reasonably well with the unseeded cases (lowest values of Δp_{tot} shown). In other words, standard scaling using the EPED1 model [25] would predict narrower pedestal widths for cases with higher neon seeding.

As a combination of the decreasing n_e pedestal and its widening, the maximum of the gradient of the electron density profile in the pedestal region for the seeded case is considerably lowered to 25% of the unseeded discharge. On the other hand, a sizable 50% increase in the maximum of the gradient of the electron temperature profile is observed despite the widening of the T_e pedestal, as shown in figure 9. The maximum of the gradient of the total pressure profile, calculated following equation (1), reflects both of these effects. Since the drop in $\nabla n_{e,|max}$ is significantly larger compared to the increase in $\nabla T_{e,|max}$, the maximum total pressure gradient is decreased by a factor of 1.5 to 2 once the lowest

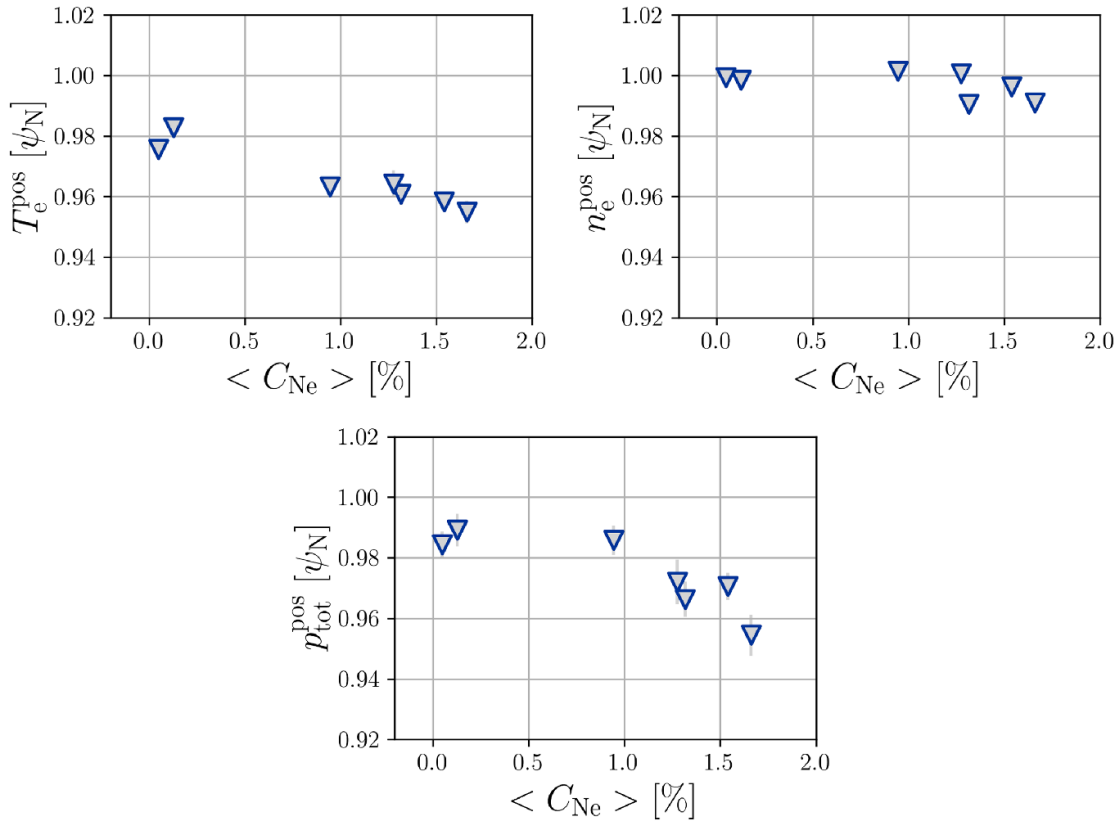

Figure 6. Dependency of the position of the maximum gradient value of kinetic plasma profiles in normalized coordinate ψ_N on the estimated neon concentration for the presented dataset. The position of the electron temperature T_e^{pos} and electron density n_e^{pos} are shown in the top row left and right and the total plasma pressure p_{tot}^{pos} at the bottom.

amount of neon seeding from the presented dataset is introduced. However, no additional decrease with the increasing neon concentration is observed. It seems more likely that the pressure gradient is stabilized and even modestly increasing for cases where the neon concentration exceeds 1.5%.

4. Pedestal stability

The pedestal stability analysis may improve our understanding of the processes occurring in the edge plasma region during pedestal creation, its development, and possibly also the mechanisms that limit its height or trigger instabilities, like ELMs, causing its collapse. The following section is focused on the examination of pedestal stability of the presented dataset using ideal MHD to study the peeling–ballooning (PB) instabilities. The key goal here is to assess the stability of the neon-seeded discharge dataset, where decreasing ELM activity with the increasing neon concentration was observed, as shown in figure 2. The PB modes have been shown to be the cause of the ELM-triggering mechanism in many machines, partially including JET-ILW [22]. However, an inconsistency between the predicted critical pressure and the experimental value was observed for a significant set of JET-ILW discharges, despite regular ELM activity being present [26]. This observation suggests that the regime of the ELM-triggering mechanism has changed or that some physical processes neglected in the ideal MHD calculation have a non-negligible impact on the ELM behavior after switching from a carbon to metallic first wall [22, 27]. At this point, it is unclear what to expect from the ideal MHD analysis of cases with sporadic or zero ELM activity in the presented dataset.

4.1. Evaluation of pedestal stability

To assess the pedestal stability of a given tokamak discharge, the main plasma parameters need to be collected (I_p, B_T, β_N, Z_{eff}, Z_{imp}, ion mass) together with the shape of the separatrix. The diagnostics results, especially the kinetic profiles, have been mapped onto the normalized poloidal flux ψ_N using the best available equilibrium from EFIT++ determined with the full set of available magnetic measurements improved by constraining the pressure profile, which has been shown to improve the computed separatrix location [28]. Fitted kinetic profiles from the pre-ELM phase (the last 30% of the ELM cycle) have

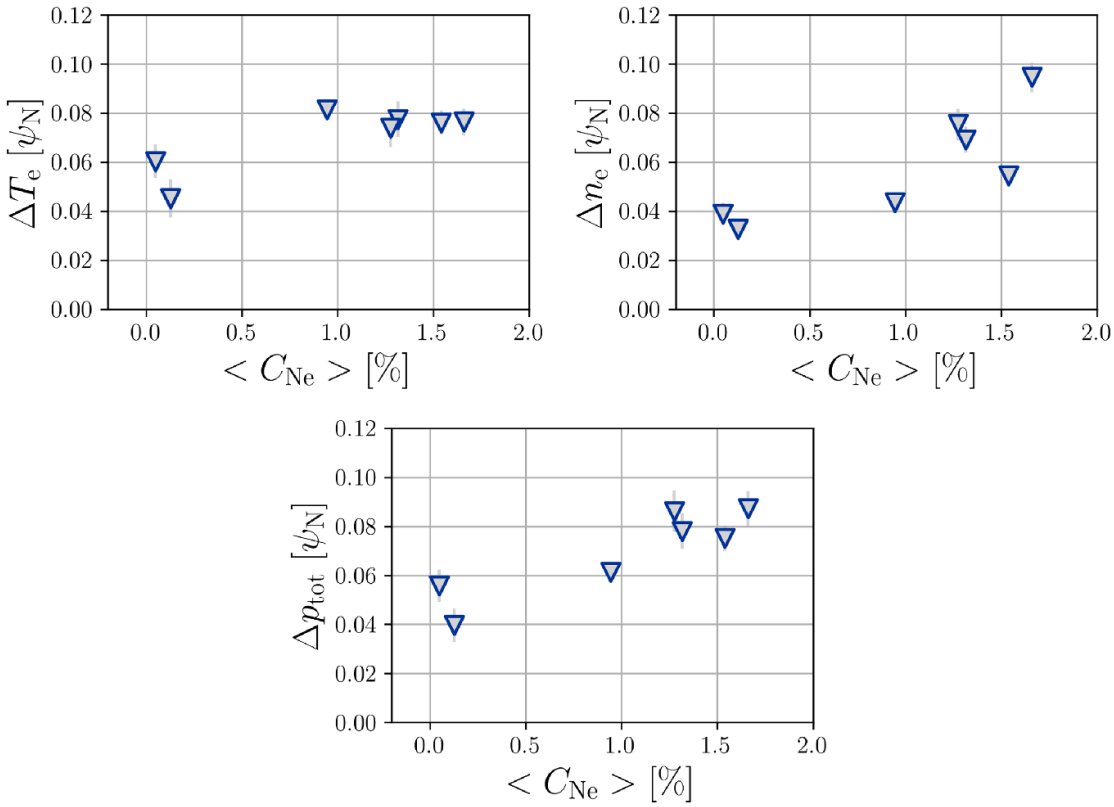

Figure 7. Dependency of the pedestal width observed on kinetic profiles of presented dataset on estimated neon concentration. Values of the width of electron temperature ΔT_e and electron density Δn_e are shown in the top row, while the total plasma pressure pedestal width Δp_{tot} is presented in the bottom row.

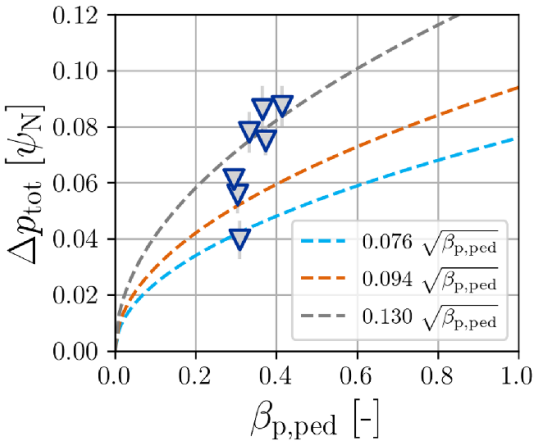

Figure 8. Scaling of the total pressure pedestal width Δp_{tot} with the poloidal β parameter evaluated at the top of the pedestal.

been used when possible. In the case of low or no ELM activity discharges, the ELM cycle condition is neglected and the selection is reduced to only the profiles with good data quality.

For the purpose of analyzing the coupled PB mode stability, the 2D ideal MHD code MISHKA has been developed [29]. MISHKA enables calculation of the growth rate of a coupled PB mode with a given toroidal mode number n for specified plasma conditions and equilibrium reconstruction. The results are then organized to produce a 2D stability diagram in the $(j_{\|} - \alpha_{max})$ space, where $j_{\|}$ is the maximal electric current in the parallel direction to the toroidal magnetic field in the pedestal region and α_{max} represents the maximum normalized pedestal pressure gradient α, defined as

$$\alpha = -\frac{1}{\pi^2}\frac{\partial V}{\partial \psi}\left(\frac{V}{2\pi^2 R_0}\right)^{1/2}\mu_0\frac{\partial p}{\partial \psi}, \tag{4}$$

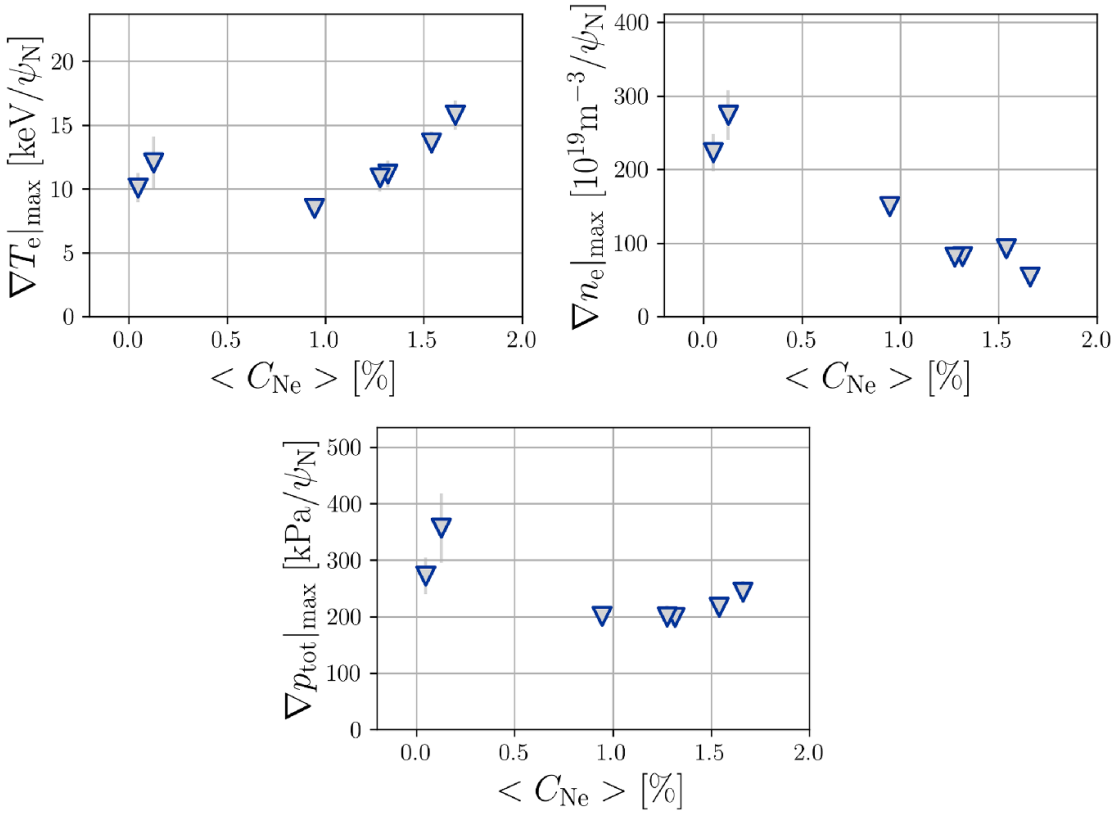

Figure 9. Dependency of the maximum gradient value of kinetic plasma profiles on estimated neon concentration for presented dataset. Maximum gradient of electron temperature T_e and electron density n_e are shown in the top row left and right, respectively, and total plasma pressure p_{tot} on the bottom row.

where V and p denote the plasma volume and pressure profiles, respectively, R_0 is the tokamak major radius, and ψ signifies the poloidal magnetic flux, with μ_0 as the vacuum permeability constant. As a first step, the experimentally obtained plasma conditions (profiles of electron temperature and density, plasma boundary, fundamental plasma parameters) are used to calculate the operational point of a given plasma state, i.e. the location in the $(j_{||} - \alpha_{max})$ space, the so-called *experimental point* (orange diamond symbol in figure 10). The (x, y) coordinates of the experimental points in the 2D stability diagram are therefore denoted as (α_{exp}, j_{exp}), respectively. The uncertainty of the experimental point position within the diagram is calculated from the uncertainty of the pedestal widths obtained during the fitting procedure, which is usually of the order of 15%–20%.

The vicinity of the experimental point is scanned in the requested range of $j_{||}$ and α_{max} by scaling the profiles of plasma current density j, electron temperature T_e ,and density n_e. Changes in the electron T_e and/or n_e result in alternating the pressure gradient α. The bootstrap current j_{bs} has a defining impact on the plasma current profile $j_{||}$ in the pedestal region, referred to as the pedestal current, since it is primarily driven by the plasma pressure gradient, apart from being decreased with the collisionality ν. Therefore, changes in the pressure profile are reflected during the scanning of the pedestal current (vertical axis in figure 10). The evaluation of the bootstrap current j_{bs} contribution to the total plasma current density profiles is carried out using the Redl formula [30].

An example of a 2D pedestal stability diagram is presented in figure 10 for two JET discharges from the analyzed dataset. The contours of the growth rate magnitude of the most unstable toroidal mode γ_{max} normalized by the Alfvén frequency ω_A at given points of the 2D scan are presented in the $(j_{||} - \alpha_{max})$ space. The boundary between the stable and unstable region, referred to as the PB stability boundary (see the black solid line in figure 10), from the PB instability point of view can be evaluated from the growth rates of the most unstable modes γ_{max} on the scanned grid once appropriate critical conditions are established. Using 3% of the Alfvén frequency ω_A as a stability criterion is a commonly used assumption, and does not have a major effect on the general results when compared with different stability conditions (such as $\gamma > 0.25\omega^*_{max}$, where ω^*_{max} is the maximum of the ion diamagnetic frequency in the pedestal region). The operation space is considered to be divided by the stability boundary into

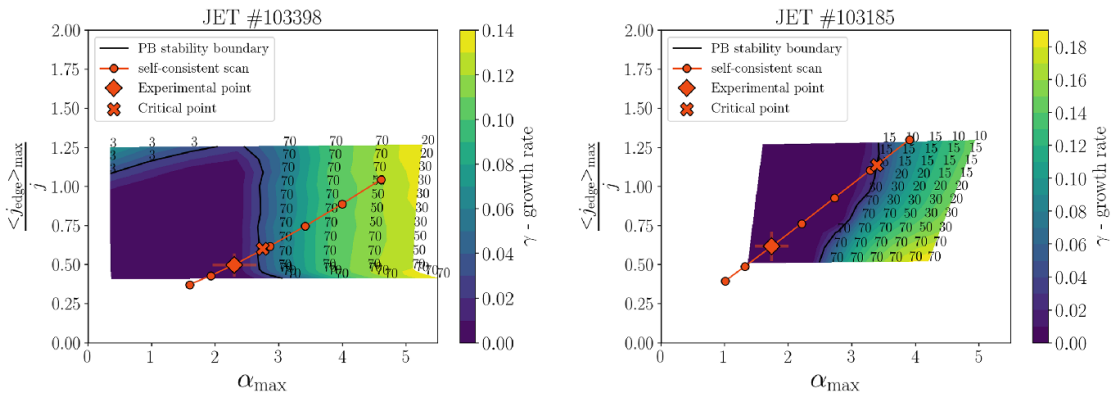

Figure 10. 2D stability diagrams calculated for two JET discharges: #103398 unseeded (left) and #103185 with Ne seeding (right).

stable (to the left) and unstable (to the right) regions. The toroidal numbers of the most unstable modes are indicated in the unstable region.

A different approach is the so-called *self-consistent scan* to obtain the 'distance' of the experimental point to the stability boundary. The height of the pedestal temperature profile is gradually scaled, while the corresponding bootstrap current is calculated for such a profile using a selected formula. It is assumed that the pedestal of the electron temperature and/or density profile, and therefore also the pressure, and corresponding current density profile would evolve naturally in this manner during the ELM cycle, and is thus considered to be self-consistent [3]. The orange line in figure 10 is a representation of the self-consistent scan within the standard 2D stability diagram. The critical point (orange cross in figure 10) is defined as the position where the growth rate exceeds the stability criterion. Throughout this work, the mode is considered unstable when its growth rate γ meets the stability condition $\gamma > 0.03\ \omega_A$. The corresponding (x, y) coordinates of the critical point in the 2D stability diagram are denoted as $(\alpha_{crit}, j_{crit})$, respectively. It is worth mentioning for clarification at this point that, within the process of the presented self-consistent stability analysis, only the height of the electron temperature and/or density pedestals is scaled, while the other profile parameters are kept fixed. This is in contrast to standard usage of the Europed model, where the widths are scaled along with the height of the pedestal.

4.2. Pedestal stability of Ne-seeded scan in deuterium for JET-ILW dataset

The position of the experimental point relative to its corresponding PB boundary in the unseeded case #103398, from the left part of figure 10, suggest that within the uncertainty it lies very close to the ideal PB boundary on the ballooning side of the diagram and can therefore be considered unstable to ballooning modes, which have a higher toroidal mode number. This means that the pedestal height is limited by the ideal PB modes, which possibly account for the ELM triggering mechanism. As a comparison, the experimental point of the most seeded case within the dataset (#103185) is located deep in the stable region with reference to the PB stability boundary, as shown in figure 10 on the right. This case can thus no longer be assumed to be limited by the ideal PB modes. This is partly expected due to the fact that in this discharge the ELM activity disappears almost completely, as can be seen from figure 2. Due to the shape of the PB boundary and the trajectory of the self-consistent scan, it is clear that the distance of the experimental point to its corresponding boundary is larger for the presented neon-seeded case. The distance can be defined as the ratio between α_{exp} and α_{crit}. In particular, $\alpha_{crit}/\alpha_{exp} \approx 1.2$ for the unseeded case and $\alpha_{crit}/\alpha_{exp} \approx 2.0$ for the most neon-seeded case.

To demonstrate the impact of neon seeding on the pedestal stability, a comparison of the experimental point positions and their corresponding PB boundaries is presented in figure 11 for multiple levels of neon concentration from the dataset having one unseeded case as a reference. In all cases, the stability limit was set to 3% of ω_A. Once neon seeding is introduced, the experimental point is shifted to lower values of the normalized pressure gradient α_{max}. This is a direct consequence of the decrease in the total pressure gradient presented in figure 9. The position of the experimental point is shifted to higher values of pedestal current, keeping the normalized pressure gradient constant within the uncertainty when increasing the neon concentration from approximately 0.4 to 0.6. This is in agreement with

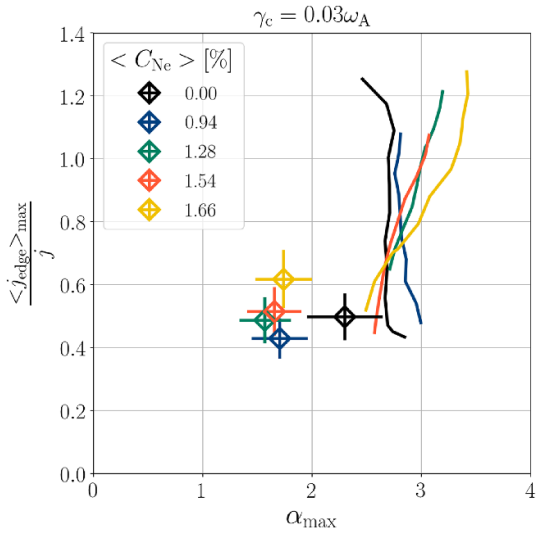

Figure 11. Comparison of the position of experimental points and the PB boundary for a set of discharges representing the presented dataset. The color of the given PB boundary corresponds to that used for showing the experimental point. The boundary was calculated using the critical growth rate equal to 3% of ω_A.

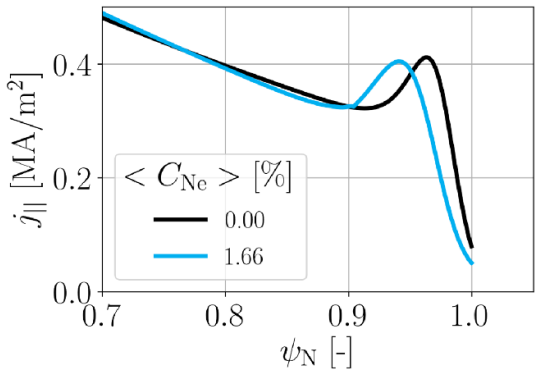

Figure 12. Comparison of the current density profiles from the Ne seeding scan showing the unseeded case #103398 and the most seeded discharge #103185.

the maximum of the pressure gradient (see figure 9) remaining relatively constant with the increasing neon concentration. The increase in the pedestal current, which is mainly composed of the bootstrap current, can be accounted for by a decrease in the pedestal collisionality ν, which should follow $\nu \propto Z_{eff}\ n_e\ T_e^{-2}$ in the *banana regime* [31]. The electron density is decreasing, while both the electron and ion temperature profiles experience an increase with the increasing neon concentration. The proportionality to Z_{eff}, which increases with the neon concentration naturally, only partially cancels out the combined effect of n_e and T_e. Moreover, the position of the bootstrap current peak shifts inward with the neon concentration due to the widening of the electron density and temperature profiles. This is illustrated in figure 12.

The stability boundaries of the entire dataset do not change significantly and always remain rather close to the unseeded pedestal boundary, especially in the closest vicinity to the experimental point at around $< j_{edge} >_{max} / j = 0.6$. An extension of the boundary in the intermediate-n PB region of the diagram ($< j_{edge} >_{max} / j \approx 1.2$) is caused by the reduction of edge collisionality during neon injection, which increases the bootstrap current and thereby reduces the local magnetic shear in the pedestal. Lower shear enhances access to second-stability ballooning regimes; thus, larger pressure gradients can be sustained before intermediate-n PB modes become unstable. It should be noted that the boundary position was determined using the Alfvén frequency criterion, and therefore the conclusions regarding the stability boundary are valid only within this framework. In order to quantify the impact of neon seeding on the pedestal stability, the distance of the experimental point to the PB stability boundary, defined as the ratio $\alpha_{crit}/\alpha_{exp}$, was calculated. Figure 13 shows the correlation between α_{exp} (a), α_{crit} (b), and

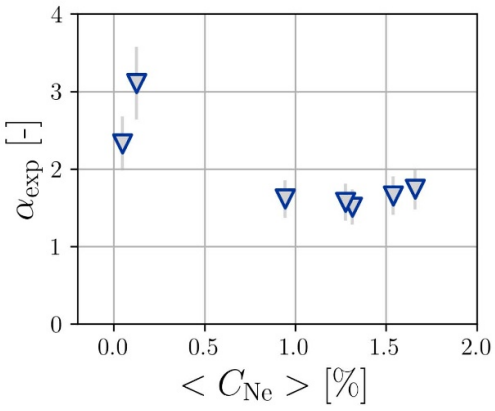

(a) Experimental maximum normalized pressure gradient.

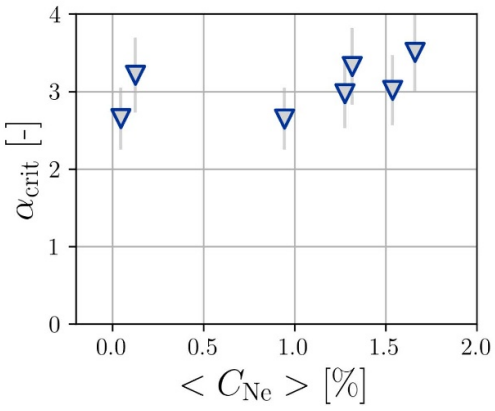

(b) Estimated critical maximum normalized pressure gradient.

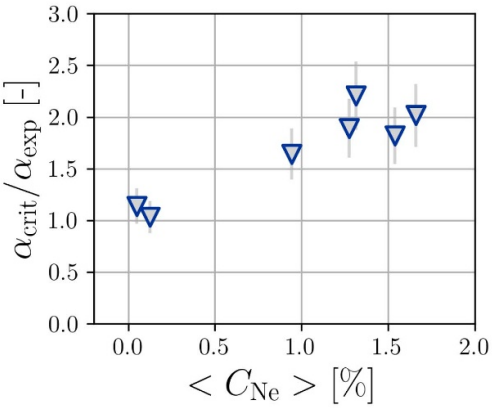

(c) Distance between the experimental point and PB boundary.

Figure 13. Correlation of pedestal stability results with neon concentration.

their ratio $\alpha_{crit}/\alpha_{exp}$ (c) versus the neon concentration. As already discussed, the total pressure gradient of the neon-seeded cases decreases by approximately 40% and remains constant throughout the presented scan as the neon is introduced, as shown in figure 13(a). The critical value of the normalized pressure gradient, α_{crit}, does not vary substantially within the dataset even for unseeded and seeded cases; see figure 13(b). Using the self-consistent scan to evaluate α_{crit} crossing the PB boundary in the intermediate-n PB region for highly seeded cases, a modest increasing trend with the neon concentration can be observed, despite being encumbered by a substantial uncertainty of up to 20%.

As a result, a significant increase in the distance with the neon concentration is observed in figure 13(c). Clearly, for both unseeded cases, $\alpha_{crit}/\alpha_{exp}$ lies close to unity, which suggests good agreement with the ideal PB model, meaning that the maximum pedestal pressure seems to be limited by PB modes. The increase in $\alpha_{crit}/\alpha_{exp}$ for the neon-seeded discharges by a factor of 2 with an increasing trend as the neon concentration reaches higher values is mainly caused by a steady drop in α_{exp} and a modest increase of α_{crit} within the seeding scan.

5. Europed predictions

The pedestals of neon-seeded discharges in deuterium appear to be stable to the ideal MHD PB modes as demonstrated in the previous section. The distance of the experimental points from the PB stability boundary with neon seeding is too large for the cases to be regarded as PB-limited, even taking significant uncertainty into consideration; see figure 13. Nonetheless, it might be interesting to compare the

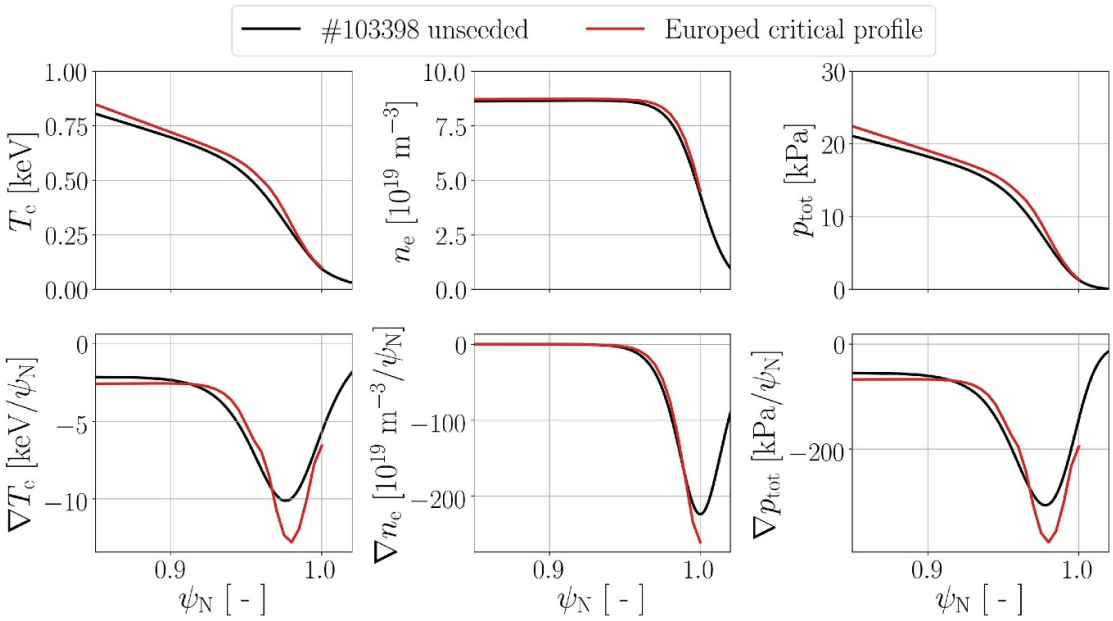

Figure 14. Comparison of experimental fitted kinetic profiles and critical profiles predicted by the Europed model. Electron temperature T_e, electron density n_e, and total pressure p_{tot} are respectively presented in the top row from left to right. The bottom row shows corresponding gradients calculated from the data shown in the top row.

experimental results with the Europed predictions. This comparison could still provide valuable information to understand the origin of the discrepancy between the experiments and modeling. It is also worth mentioning that in many earlier cases, Europed was still able to predict the pedestal height reasonably well, despite the pedestal being not limited by ideal MHD [32]. As presented in figure 8, regardless of the choice of scaling coefficient $c_{\Delta p_{tot}}$, a satisfactory match of the experimental pedestal pressure widths is not achieved, especially for higher neon concentration level cases. It is possible that these two opposing effects would cancel each other, which would in the end provide reasonable predictions for the pedestal heights using the Europed model.

5.1. Europed approach

The Europed [32] code implements the EPED model [24]. EPED is a semi-empirical pedestal transport model developed to predict the edge pressure pedestal height and width in H-mode tokamak plasmas. It incorporates the interplay between PB MHD stability limits and kinetic ballooning mode turbulence thresholds. Europed has been validated against the experimental results from devices such as JET [32, 33] and ASDEX Upgrade [34, 35], providing a computationally efficient tool for scenario development and integrated modeling. In Europed, the constant used in the width expression can be used as a free parameter. In this work, the constant was fine-tuned to have a good agreement with the unseeded pedestal, and was then kept constant throughout all of the following scans.

Firstly, the best achievable agreement between the pedestal structure of the experimental and the predicted profiles was found by tailoring the Europed input settings for the reference unseeded case #103398. It is worth mentioning that the best match was found for the pedestal width scaling coefficient $c_{\Delta p_{tot}} = 0.094$, which is larger compared to the value of 0.076 developed with the EPED model [24] for standard H-mode operation on multiple tokamak devices [25]. More details of the setup can be found in the appendix. The comparison of the profiles is presented in figure 14. The agreement is very good concerning the profiles of T_e, n_e, and p_{tot} in terms of pedestal height and position. When looking at the gradients, the maximum critical gradients overestimate the experimental ones by approximately 20%. As discussed in [24], this is the typical agreement expected in the EPED1 predictions.

As the next step, the neon seeding part of the discussed scan was simulated by varying parameters to capture the changes caused by the increasing neon concentration. The optimized Europed setup used to find a proper match for the predicted critical and the experimental profiles for the reference unseeded case was used as a starting point. The parameters scanned are the effective charge Z_{eff}, pedestal density $n_{e,ped}$, and confinement parameter β_N. Z_{eff} was changed because it increases with the neon seeding as a direct effect of the increasing neon content. However, changing Z_{eff} alone proved to be insufficient. This is because both $n_{e,ped}$ and β_N, the other direct input parameters of Europed, change with the increasing

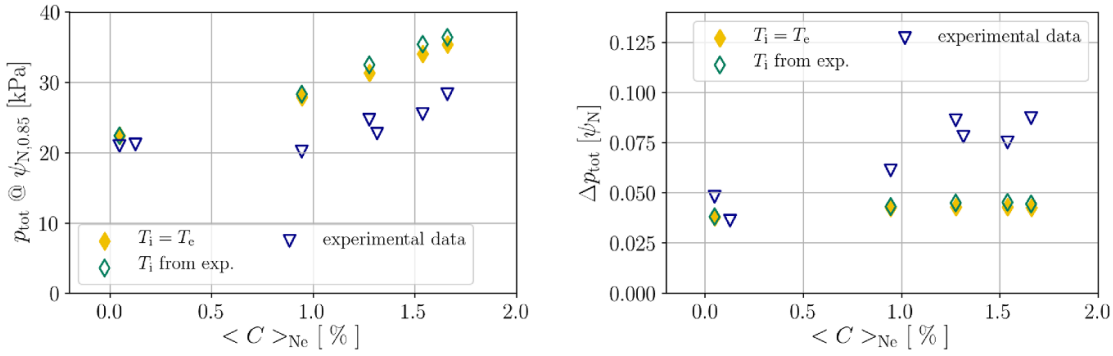

Figure 15. Parameters of predicted profiles using Europed model by matching experimental values of Z_{eff}, $n_{e,ped}$, and β_N to the best match found for the unseeded case #103398 for both variants when experimental ion temperature profile T_i was taken and when $T_i = T_e$ was assumed. Comparison is presented for values of total pressure pedestal height p_{tot} and total pressure pedestal width Δp_{tot} depending on the averaged neon concentration.

neon concentration. These parameters can be estimated for an intended discharge by means of other models, and in this way the pedestal performance can be predicted, accounting also for the impact of neon seeding once the reference discharge is provided.

5.2. Scan experimental parameters

The resulting predictions for the total pressure pedestal are presented in figures 15 and 16 for the total pressure profile parameters. The total pressure pedestal height appears to be significantly overestimated by a systematic difference of 30%–40% when compared to the experimental values, which correspond to a rather constant difference of 6–8 kPa for all seeded cases, as shown in figure 15. However, a good qualitative agreement can be seen, with the predicted p_{tot} increasing with the increasing neon concentration. On the other hand, the total pressure pedestal widths seem to be significantly underpredicted, in addition to being constant with the increasing neon concentration. The experimental data points suggest substantial widening of the total pressure pedestal widths, which is not captured properly by the presented method.

As can be seen from figure 15, both T_i variants result in comparable predictions for the pedestal heights and widths with the increasing neon concentration. This is beneficial for the modeling approach, as the assumptions on T_i are not essential for the predictions of these plasmas.

In figure 16, direct comparisons of the Europed predictions (denoted by subscript 'EUROPED') and the experiments (subscript 'exp') for total pressure pedestal heights and widths are made. The good agreement of the prediction for the unseeded reference case is disturbed once neon seeding is applied, and both the pedestal pressure height and width start to deviate from the ideal 1:1 line.

In conclusion, the general trend of increasing the total pressure pedestal height with the increasing neon concentration is captured; however, the predictions exhibit a significant absolute offset of 6–8 kPa. The total pressure pedestal widths are underpredicted and show no increasing trend with the neon seeding. Comparable results were obtained when the second unseeded reference discharge #105625 was used as a starting point and the whole process was repeated.

5.3. Individual scans

In order to evaluate the effects of the plasma parameters scanned in the previous part, individual scans were performed. This was done to identify the parameter that plays the main role in qualitatively reproducing the experimental correlation presented in figure 15. The results are shown in figure 17. In all three frames of figure 17, for comparison, the full yellow diamonds show the full scan described above and the blue triangles as the experimental data, both presented in figure 15. Then, figure 17(a) shows the effect of Z_{eff}. Increasing only Z_{eff} (green diamonds) has no significant effect on the predictions. Figure 17(b) shows the effect of only $n_{e,ped}$. The reduction of $n_{e,ped}$ (light blue diamonds) leads to a weak increase in the p_{tot} predictions, which does not capture its increasing trend with the decreasing $n_{e,ped}$. Finally, figure 17(c) shows the impact of the β_N parameter (pink diamonds). It is clear that the main role is played by the β_N parameter.

To qualitatively reproduce the trend of increasing total pressure with the neon concentration, the correct value of β_N is necessary. This suggests that integrated core–pedestal modeling is vital to correctly predict the qualitative behavior of neon-seeded pedestals.

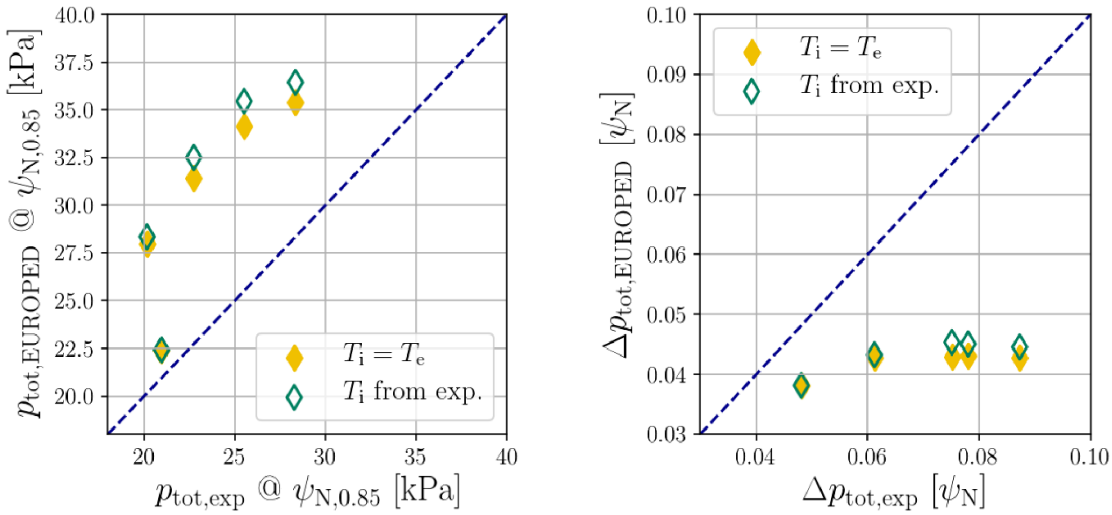

Figure 16. Direct comparison of experimental and predicted values using Europed model by matching experimental values of Z_{eff}, $n_{\mathrm{e,ped}}$, and β_N to the best match found for the unseeded case #103398 for both variants when experimental ion temperature profile T_i was taken and when $T_\mathrm{i} = T_\mathrm{e}$ was assumed. Comparison is presented for values of total pressure p_{tot} pedestal height and total pressure pedestal width Δp_{tot}.

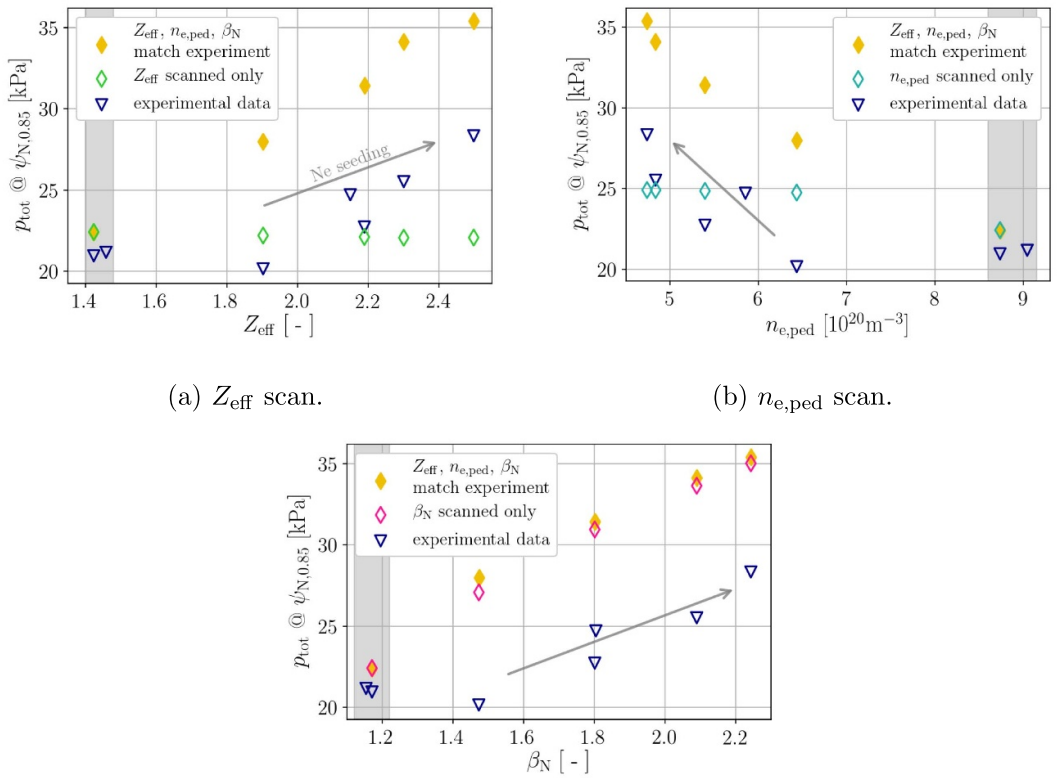

(a) Z_{eff} scan.

(b) $n_{\mathrm{e,ped}}$ scan.

(c) β_N scan.

Figure 17. Parameters of predicted profiles using Europed model by matching individual values of selected parameter to the experimental values of Z_{eff} (a), $n_{\mathrm{e,ped}}$ (b), and β_N (c) to the best match found for the unseeded case #103398. Comparison is presented for values of total pressure p_{tot} pedestal height depending on the scanned parameter. The gray arrow represents increasing neon concentration within the seeding scan. Gray shaded area is used to highlight the unseeded discharges.

6. Discussion and conclusion

6.1. Discussion

The present study extends earlier JET-ILW impurity seeding investigations by systematically analyzing the response of the pedestal structure and stability to increasing levels of neon seeding in JET-ITER baseline deuterium plasmas. The results can be contrasted with previous conventional gas-fueled JET-ILW H-mode discharges. In typical JET-ILW gas puff scans, increasing the deuterium fueling rate tends to increase the separatrix density and flatten the density gradient at the edge, which, combined with a lower pedestal temperature, leads to reduced pedestal pressure and stored plasma energy [22, 36]. These trends are well documented in the JET-ILW pedestal database [22] and reflect the outward shift of the density pedestal with higher fueling. In comparison, the neon-seeded cases presented in this work exhibit the opposite behavior: despite the deuterium gas puff being held constant and the increasing relative shift, adding neon improves the pedestal performance. In this scan, we observe significantly higher electron and ion temperature pedestal heights (T_e nearly doubles to ∼1.5 keV, T_i up to 2 keV) while the density pedestal height decreases from $\sim 9 \cdot 10^{19}\,\mathrm{m}^{-3}$ to $\sim 6 \cdot 10^{19}\,\mathrm{m}^{-3}$ at the highest neon concentration levels, as shown in figure 5. As a result, the electron pressure p_e increases by ∼30% and the ion pressure p_i by almost 50% with the assumption that the actual impurity mix is characterized only by the main impurity species ($Z_{imp} = 2$ for unseeded and $Z_{imp} = 10$ for seeded cases). Despite the much larger impact of neon seeding on the T_i pedestal height, which increases by up to a factor of 2, compared to 1.5 for T_e, the overall contributions of the electron and ion pressure to the total pressure are comparable. This is due to compensation by the ion density dilution as Z_{eff} increases, in addition to the medium-Z impurity presence ($Z_{imp} = 10$). The net effect can be established as approximately a 50% increase in the total pedestal pressure relative to the unseeded reference, which is a contrast to pure fueling scans, where such a pedestal pressure increase at constant power is not achieved. Moreover, neon seeding causes a significant impact on the pedestal widths of T_e, n_e, and p_{tot}, as presented in figure 7. All expand significantly with the neon concentration by approximately a factor of two when comparing the most seeded case with the reference. In standard gas-fueled discharges, by comparison, the pedestal widths often show little increase or even a slight decrease with higher fueling, and the pedestal tends to shift outward rather than broaden [36].

Alongside the change in structure, the pedestal stability in neon-seeded discharges shows a clear shift when compared to standard JET behavior. To evaluate the pedestal stability, we employed an ideal MHD stability approach (using the MISHKA code [29]) to assess the position of experimental points at the PB boundary. This method proved reasonably applicable as it clearly distinguished the unseeded and neon-seeded regimes. Unseeded JET-ITER baseline pedestals are usually near the ideal PB stability limit [1, 7]. The operating point lies close to the calculated PB boundary with $\alpha_{crit}/\alpha_{exp} \approx 1$ indicating that the pedestal pressure gradient is at the threshold of PB instability, as presented in figure 13. However, with neon seeding, the pedestal moves further away from the PB boundary into the stable region. We find that the experimental normalized pressure gradient (α_{exp}) decreases by ∼40% as neon is introduced, while the PB critical gradient (α_{crit}) remains roughly constant. As a result, the distance from the PB boundary almost doubles (from $\alpha_{crit}/\alpha_{exp} \approx 1.2$ in unseeded conditions to ∼2.0 at the highest neon concentration). In other words, the neon-seeded pedestals are considered PB-stable and no longer limited by ideal PB modes.

As discussed above, the separatrix temperature was fixed at $T_{e,sep} = 100$ eV in order to maintain consistency throughout this contribution due to the large uncertainty in the position of the pedestal of the kinetic profiles. This approach also enables a better comparison with the previously performed analysis of pedestal structure and ideal MHD stability, presented in [7, 21]. Sensitivity tests were performed in order to assess the possible undesirable impacts on the pedestal stability analysis results. Different values of the separatrix temperature were selected, $T_{e,sep} = 80$–150 eV, and the radial extent of all the kinetic profiles was altered accordingly. It is shown that the impact on the shape and position of the PB boundary is not significant in the closest vicinity to the experimental point. In particular, the ratio $\alpha_{crit}/\alpha_{exp}$ remains in the range 1.1–1.2 for the unseeded case and 1.8–2.1 for the most seeded case and, thus, does not change significantly with $T_{e,sep}$ and remains within the uncertainty of the original results. Therefore, from the perspective of the ideal PB stability analysis, the conclusions are unchanged with respect to the separatrix temperature assumption.

Simultaneously, the relative shift, $n_e^{pos} - T_e^{pos}$, increases with the neon concentration, as the position of the temperature pedestal moves inward, keeping the peak density gradient position constant. It is observed and well documented that $\alpha_{crit}/\alpha_{exp}$ is positively correlated with the relative shift [22], which is in line with the presented results. In contrast, the fuel gas puff was kept constant in the presented dataset, which seems to be tied with the relative shift in [22]. This would suggest a different relative

shift generation mechanism connected with the impurity seeding. However, the causality of the relative shift and $\alpha_{crit}/\alpha_{exp}$ with the neon seeding remains unclear. Consistent with this, ELM activity observations suggest that the ELMs effectively disappear in the most strongly seeded discharges, as shown in figure 2. This observed transition is in qualitative agreement with earlier findings from JET experiments with neon seeding. In particular, it was reported [1] that at moderate neon levels (∼1% Ne concentration) in a previous JET-ITER baseline scenario at 2.5 MA, 2.7 T at high triangularity, the pedestal operational point remained just ∼20% below the PB boundary while the pedestal width increased, yielding a higher pedestal pressure than in the unseeded case. A comparable reduction in ELM frequency and size, approaching small/no-ELM operation, also reported in [1], is consistent with the behavior observed here. Our results extend the neon seeding range into a fully ELM-suppressed domain at $q \approx 3$. In summary, based on the analysis presented in this contribution, ideal PB-stable pedestals were observed while maintaining a high pedestal total pressure and enhanced confinement quality. This demonstrates that with sufficiently strong neon seeding at higher heating power, JET plasmas can undergo a transition to an ideal PB-stable regime without suffering a collapse in pedestal performance.

Moreover, the Europed model could still be used to make quantitative comparisons to the experiment. We found that with suitable tuning, it could reproduce the general trend of increasing pedestal pressure height with neon, despite a fixed overshoot of 6–8 kPa, and even match the unseeded case reasonably well. However, important limitations were recognized when applied to strongly neon-seeded pedestals. First, the standard EPED scaling for the pedestal width no longer seems to be valid, and using the original scaling coefficient ($c_{\Delta p_{tot}} \approx 0.076$) substantially underpredicted the width of the pedestal observed in the experiment. We had to increase the width coefficient ($c_{\Delta p_{tot}} \approx 0.094$) in the Europed settings to obtain a better agreement with the measured widths. This rather empirical adjustment suggests that the physics of pedestal broadening with neon seeding are not captured by the model assumptions we used. Second, the ideal MHD stability code itself cannot address non-ideal effects that might be relevant in these plasmas. For instance, in the cases with the highest neon concentrations, the pedestal is far from the ideal PB limit; therefore, factors like finite diamagnetic stabilization or resistive modes could be setting a separate limit to pedestal gradients. The presented stability analysis assumes that only the profiles inside the confined plasma region defined by the separatrix have any impact on the stability. However, changes in the scrape-off layer or neutral fueling, which are clearly affected by neon seeding via cooling or detachment, might influence the pedestal conditions, which is outside the scope of the ideal PB model. It must be recognized that the absence of ELMs in these discharges implies that some other mechanism is constraining the pedestal. The framework for the stability evaluation used in this work can only conclude that the observed mode is not an ideal PB mode. In summary, the ideal MHD pedestal modeling served to quantify how far the neon cases moved into the stable domain and to compare with earlier JET studies. Future work may require incorporating non-ideal effects or advanced edge turbulence simulations to fully explain what saturates the pedestal in these ELM-free, neon-seeded plasmas.

6.2. Conclusion

As shown in previous works [1, 7] the increase in the neon concentration leads to an increase in pedestal total pressure, thus improving the pedestal performance in JET deuterium H-mode discharges. The height of the p_{tot} pedestal increases with increasing seeding due to broadening of the p_{tot} pedestal width, while the total pressure gradient decreases. The widening of the pedestal pressure is mainly caused by increasing the electron temperature pedestal width. The widening of the electron density width plays a negligible role because the peak density gradient position is near or outside the separatrix, where the pressure gradient is already very low. Both the T_e and T_i pedestals rise significantly with neon, more than compensating for the moderate decrease in pedestal density, which as a result causes an increase in the total pedestal pressure by approximately 50% relative to the reference unseeded plasmas. Even though the ion temperature undergoes a significantly larger increase with the neon concentration, due to the ion density dilution at higher impurity levels, the electron and ion pressure contributions to the total pressure pedestal are comparable.

With neon seeding, the normalized total pedestal pressure gradient α_{exp} decreases by ∼40% from the average ∼2.7 to ∼1.6, but the ideal MHD pedestal stability boundary does not change significantly. From the point of view of pedestal stability, by increasing the neon seeding, the pedestal goes from being limited by ideal PB modes to being stable to ideal PB modes. Further investigations into pedestal stability showed that Europed predictions underestimate the pedestal width, and because the pedestal is stable to ideal MHD, the pedestal gradients are overpredicted. However, the two compensate each other, and overall, the predicted pedestal height is in reasonable agreement with the experimental results. Qualitatively, the observed increasing trend of the total pressure pedestal height with neon seeding

is accurately captured by Europed. Our results suggest that within the Europed framework, increasing β_N has the highest impact on the total pressure predictions. This suggests that, in order to utilize Europed for the estimation of the critical pedestal parameters, integrated core–pedestal modeling is essential to provide the correct predictions of plasma performance.

Data availability statement

The data that support the findings of this study are available upon reasonable request from the authors.

Acknowledgments

This work has been carried out within the framework of the EUROfusion Consortium, partially funded by the European Union via the Euratom Research and Training Programme (Grant Agreement No. 101052200–EUROfusion). The Swiss contribution to this work has been funded by the Swiss State Secretariat for Education, Research and Innovation (SERI). Views and opinions expressed are however those of the author(s) only and do not necessarily reflect those of the European Union, the European Commission or SERI. Neither the European Union nor the European Commission nor SERI can be held responsible for them. This work was supported by the MEYS Project No. 9D22001.

Appendix. Europed setup to match unseeded case

In order to match the experimental profile with the critical profile predicted by Europed, the following setup was selected after extensive parameter and sensitivity scans. If the data are available, the physical parameters of the simulation are taken directly from the experimental measurements. Numerical (technical) parameters that are optimized to match the experimental profiles are summarized in the following table:

Parameter	Value	Description
beta_exponent	0.5	Exponent in the width scaling formula
density_shift	0.02 ψ_N	Outward density shift relative to temperature
nesep_multip	0.0	Ratio $n_{e,sep}$ / $n_{e,ped}$ in this setup
pedestal_width_ratio	1.2	Ratio of ΔT_e / Δn_e in ψ_N
width_const	0.094	Coefficient in the width scaling formula

ORCID iDs

M Šos 0000-0003-3546-7084
L Frassinetti 0000-0002-9546-4494
B Chapman-Oplopoiou 0000-0001-9879-2285
S Saarelma 0000-0002-6838-2194
S Wiesen 0000-0002-3696-5475
B Labit 0000-0002-0751-8182
A Kappatou 0000-0003-3341-1909
D Keeling 0000-0002-3581-7788
N Vianello 0000-0003-4401-5346
M Wischmeier 0000-0002-3065-027X
A Boboc 0000-0001-8841-3309
J M Fontdecaba Climent 0000-0001-7678-0240
E Litherland-Smith 0009-0000-0587-2930
S Menmuir 0000-0003-3250-0256

References

[1] Giroud C *et al* (JET Contributors) 2021 High performance ITER-baseline discharges in deuterium with nitrogen and neon-seeding in the JET-ILW *28th IAEA Fusion Energy Conf. (Nice, France, 10 May–15 May 2021)*
[2] Dunne M G 2016 Impact of impurity seeding and divertor conditions on transitions, pedestal structure and ELMs *Nucl. Fusion* **57** 025002
[3] Saarelma S, Järvinen A, Beurskens M, Challis C, Frassinetti L, Giroud C, Groth M, Leyland M, Maggi C and Simpson J 2015 The effects of impurities and core pressure on pedestal stability in Joint European Torus (JET) *Phys. Plasmas* **22** 056115

[4] Hughes J W et al 2011 Power requirements for superior H-mode confinement on Alcator C-Mod: experiments in support of ITER Nucl. Fusion 51 083007
[5] Lan H, Osborne T H, Groebner R J, Snyder P B, Xu G S, Grierson B A, Victor B S, Leonard A W, Wang H Q and (the DIII-D Team) 2020 H-mode pedestal improvements with neon injection in DIII-D Nucl. Fusion 60 056013
[6] Wang H Q et al 2023 Study on divertor detachment and pedestal characteristics in the DIII-D upper closed divertor Nucl. Fusion 63 046004
[7] Giroud C et al (JET Contributors) 2024 The core-edge integrated neon-seeded scenario in deuterium-tritium at JET Nucl. Fusion 64 106062
[8] Giroud C et al 2024 High-current neon-seeded ITER baseline scenario in JET D and D-T 28th PSI Conf.
[9] Marin M, Citrin J, Giroud C, Bourdelle C, Camenen Y, Garzotti L, Ho A and Sertoli M (JET Contributors) 2022 Integrated modelling of neon impact on jet H-mode core plasmas Nucl. Fusion 63 016019
[10] Carvalho I S et al (JET Contributors and the EUROfusion Tokamak Exploitation Team) 2024 Neon seeded ITER baseline scenario experiments in JET D and D-T plasmas 50th EPS Conf. on Plasma Physics, 2024 (European Physical Society (EPS))
[11] Drenik A et al (the ASDEX-Upgrade team and the EUROfusion MST1 team) 2019 Evolution of nitrogen concentration and ammonia production in N2-seeded H-mode discharges at ASDEX Upgrade Nucl. Fusion 59 046010
[12] Delabie E et al (EUROfusion Tokamak Exploitation Team and JET Contributors) 2024 The cxsfit spectral fitting code: past, present and future Rev. Sci. Instrum. 95 083536
[13] Thorman A, Litherland-Smith E, Menmuir S, Hawkes N, O'Mullane M, Delabie E, Lomanowski B, Fontdecaba J M and Scully S (JET Contributors) 2021 Visible spectroscopy of highly charged tungsten ions with the jet charge exchange diagnostic Phys. Scr. 96 125631
[14] Leoni C et al (JET Contributors and the EUROfusion Tokamak Exploitation Team) 2025 Effects of Neon seeding on density profiles and particle sources in the Integrated Scenario at the Joint European Torus Proc. 51st EPS Conf. on Plasma Physics, (Vilnius, Lithuania, 7 July–11 July 2025) (European Physical Society)
[15] Giroud C et al 2025 High-performance ELM-free semi-detached scenario sustained at high-current in JET DTE3 30th IAEA Fusion Energy Conf.
[16] Pasqualotto R, Nielsen P, Gowers C, Beurskens M, Kempenaars M, Carlstrom T and Johnson D (JET-EFDA Contributors) 2004 High resolution Thomson scattering for Joint European Torus (JET) Rev. Sci. Instrum. 75 3891–3
[17] Hawkes N C, Delabie E, Menmuir S, Giroud C, Meigs A G, Conway N J, Biewer T M and Hillis D L (JET Contributors) 2018 Instrumentation for the upgrade to the JET core charge-exchange spectrometers Rev. Sci. Instrum. 89 10D113
[18] Menmuir S, Giroud C, Biewer T M, Coffey I H, Delabie E, Hawkes N C and Sertoli M (JET EFDA Contributors) 2014 Carbon charge exchange analysis in the ITER-like wall environment Rev. Sci. Instrum. 85 11E412
[19] Frassinetti L, Beurskens M N A, Scannell R, Osborne T H, Flanagan J, Kempenaars M, Maslov M, Pasqualotto R and Walsh M (JET-EFDA Contributors) 2012 Spatial resolution of the JET Thomson scattering system Rev. Sci. Instrum. 83 013506
[20] Groebner R J et al 2001 Progress in quantifying the edge physics of the H-mode regime in DIII-D Nucl. Fusion 41 1789
[21] Frassinetti L et al 2019 Role of the pedestal position on the pedestal performance in AUG, JET-ILW and TCV and implications for ITER Nucl. Fusion 59 076038
[22] Frassinetti L et al (JET Contributors) 2020 Pedestal structure, stability and scalings in jet-ilw: the eurofusion JET-ILW pedestal database Nucl. Fusion 61 016001
[23] Silvagni D et al 2025 The separatrix electron density in JET, ASDEX upgrade and Alcator C-Mod H-mode plasmas: a common evaluation procedure and correlation with engineering parameters Nucl. Mater. Energy 42 101867
[24] Snyder P B, Groebner R J, Hughes J W, Osborne T H, Beurskens M, Leonard A W, Wilson H R and Xu X Q 2011 A first-principles predictive model of the pedestal height and width: development, testing and ITER optimization with the EPED model Nucl. Fusion 51 103016
[25] Snyder P B et al 2009 Pedestal stability comparison and ITER pedestal prediction Nucl. Fusion 49 085035
[26] Maggi C F et al 2017 Studies of the pedestal structure and inter-ELM pedestal evolution in JET with the ITER-like wall Nucl. Fusion 57 116012
[27] Nyström H, Frassinetti L, Saarelma S, Huijsmans G T A, Perez von Thun C, Maggi C F and Hillesheim J C (JET contributors) 2022 Effect of resistivity on the pedestal MHD stability in JET Nucl. Fusion 62 126045
[28] Szepesi G, Appel L C, de la Luna E, Frassinetti L, Gaudio P, Gelfusa M, Gerasimov S, Hawkes N C, Sertoli M and Terranova D (JET contributors) 2021 Advanced equilibrium reconstruction for JET with EFIT++ 47th EPS Plasma Physics Virtual Conf. (21–25 June 2021) p 3.1037
[29] Mikhailovskii A B, Huysmans G T A, Kerner W O K and Sharapov S E 1997 Optimization of computational MHD normal-mode analysis for tokamaks Plasma Phys. Rep. 23 844–57
[30] Redl A, Angioni C, Belli E and Sauter O 2021 A new set of analytical formulae for the computation of the bootstrap current and the neoclassical conductivity in tokamaks Phys. Plasmas 28 022502
[31] Sauter O, Angioni C and Lin-Liu Y R 1999 Neoclassical conductivity and bootstrap current formulas for general axisymmetric equilibria and arbitrary collisionality regime Phys. Plasmas 6 2834–9
[32] Saarelma S, Frassinetti L, Bilkova P, Challis C D, Chankin A, Fridström R, Garzotti L, Horvath L and Maggi C F (JET Contributors) 2019 Self-consistent pedestal prediction for JET-ILW in preparation of the DT campaign Phys. Plasmas 26 072501
[33] Stefanikova E, Frassinetti L, Saarelma S, Perez von Thun C and Hillesheim J C 2020 (JET contributors) Change in the pedestal stability between JET-C and JET-ILW low triangularity peeling-ballooning limited plasmas Nucl. Fusion 61 026008
[34] Alvarez A P, Ho A, Järvinen A, Saarelma S and Wiesen S (JET Contributors and the ASDEX Upgrade Team) 2024 EuroPED-NN: uncertainty aware surrogate model Plasma Phys. Control. Fusion 66 095012
[35] Pamela S J P et al 2016 Multi-machine modelling of ELMs and pedestal confinement: from validation to prediction Proc. 26th IAEA Fusion Energy Conf.
[36] Stefanikova E et al (JET contributors) 2018 Effect of the relative shift between the electron density and temperature pedestal position on the pedestal stability in JET-ILW and comparison with JET-C Nucl. Fusion 58 056010